Ocean Sci. Discuss., 11, 753–788, 2014
www.ocean-sci-discuss.net/11/753/2014/
doi:10.5194/osd-11-753-2014

Ocean Science
Discussions
Open Access

Dynamics of turbulent western boundary currents at low latitude in a shallow water model

C. Q. C. Akuetevi[1,2] **and A. Wirth**[1]

[1]Univ. Grenoble Alpes, CNRS, LEGI UMR5519, Grenoble, France
[2]Univ. Grenoble Alpes, CNRS, LGGE UMR5183, Grenoble, France

Received: 19 December 2013 – Accepted: 11 February 2014 – Published: 5 March 2014

Correspondence to: C. Q. C. Akuetevi (cyrille.akuetevi@legi.grenoble-inp.fr)

Published by Copernicus Publications on behalf of the European Geosciences Union.

Abstract

The dynamics of low latitude turbulent western boundary currents, subject to two different types of idealized wind forcing, Monsoon Wind and Trade Wind, is considered using numerical results from integrations of a reduced gravity shallow-water model. For viscosity values of 1000 $m^2 s^{-1}$ and above, the boundary layer dynamics compares well to the analytical solutions of the Munk-layer and the inertial-layer, derived from quasigeostrophic theory. Modifications due to variations in the layer thickness (vortex stretching) are only important close to the boundary. When the viscosity is reduced the boundary layer becomes turbulent and coherent structures in form of anticyclonic eddies, bursts (violent detachments of the viscous sub-layer) and dipoles appear. Three distinct boundary layers emerge, the viscous sub-layer, the advective boundary layer and the extended boundary layer. The first is characterized by a dominant vorticity balance between the viscous transport and the advective transport of vorticity. The second by a balance between the advection of planetary vorticity and the advective transport of relative vorticity. The extended boundary layer is the area to which turbulent motion from the boundary extends. The scaling of the three boundary layer thicknesses with viscosity is evaluated.

A pragmatic approach to determine the eddy viscosity diagnostically for coarse resolution numerical models is proposed.

1 Introduction

Strong western boundary currents are a dominant feature of the worlds oceans. They are also present at low latitudes in the Atlantic and the Indian ocean, where they are called the North Brazil current and the Somali Current, respectively. In both cases strong anticyclonic eddies are observed (Richardson et al., 1994; Schott and McCreary, 2001; Wirth et al., 2001). There are however substantial differences between the two cases. One is the forcing by the wind stress field. In the equatorial

OSD
11, 753–788, 2014

Atlantic the trade winds are the major force. Whereas in the Indian Ocean the seasonally reversing Monsoon winds dominate. Another difference is the latitudinal inclination of the coast line, it is westward in the Atlantic Ocean and eastward in the Indian Ocean.

There is a large number of numerical work on the dynamics of the Somali current and the north Brazil current with a realistic coast line and topography. With the exception of the pioneering work by Edwards and Pedlosky (1998a, b) on the deep western boundary current and by Fox-Kemper (2005) on the dynamics of single and multiple gyres in a barotropic constant depth β-plane model, idealized low latitude western boundary currents have so far not been studied extensively. The above mentioned research was directed towards a detailed determination of the vorticity balances, fluxes and stability. Indeed, numerical evidence from idealized experiments on the subject with a turbulent boundary layer is scant. The present work is directed towards the determination of the turbulent structures, the fluxes and balances in low latitude western boundary currents, subject to two types of wind forcing, representing the trade wind and the Monsoon wind fields. The near western boundary region is the origin of a substantial part of turbulent kinetic energy production in the domain. It is an area of intense up-welling (Schott and McCreary, 2001; Wirth et al., 2001) and of biological production (Kawamiya and Oschlies, 2003).

To the best of our knowledge there is so far no description or theory of near wall turbulence in the western boundary current, that goes beyond the synoptic eddies. Even for oceanic western boundary currents in general the quantitative description is mainly based on laminar Munk-layer, inertial-layer theory and the analysis of their stability (see e.g. Edwards and Pedlosky, 1998b; Ierly and Young, 1991). This is in stark contrast to engineering fluid dynamics, where the turbulent boundary layer theory is the leading domain since its birth in the beginning of the 20th century (Prandtl, 1904). In the present work we focus on the dynamics of low latitude turbulent western boundary currents in a highly idealized configuration, to determine its structure, its dependence on the Reynolds number, by varying the viscosity between experiments, and its response to distinct wind forcing. The experimental set-up comprises essential

OSD
11, 753–788, 2014

prerequisites such as a fine resolution throughout the domain and long-time integrations to obtain statistically converged results.

The physical situation considered, the mathematical model to study its dynamics and its numerical implementation are discussed in the next section. Results on the taxonomy of the coherent structures, the turbulent fluxes, their parameterization and the vorticity balance are given in Sect. 4 and discussed in Sect. 5.

2 The Model

2.1 The physical problem considered

To consider the dynamics of low latitude turbulent boundary currents, with an emphasis on the Atlantic and the Indian Ocean, we constructed a highly idealized version of them. The basin is a rectangular box spanning from 1000 km south of the equator to 3000 km north of it ($L_y = 4000$ km) and it extends $L_x = 6000$ km in the zonal direction. The Coriolis parameter varies linearly with latitude $f = \beta y$, with $\beta = 2 \times 10^{-11} \mathrm{m}^{-1} \mathrm{s}^{-1}$. This geometry is usually referred to as the equatorial β-plane. We further suppose that the dynamics considered is this of an homogeneous fluid layer of an average thickness of $H = 200$ m which superposes a constant density motion-less fluid layer of infinite depth. The density difference between the layers is expressed by the reduced gravity $g' = 3 \times 10^{-2} \mathrm{m\,s}^{-2}$. These numbers are inspired by the water-mass properties in the Indian Ocean. The layer is forced by a wind shear at its surface. Two types of wind shear are considered, an equatorial easterly trade wind (TW) and a Monsoon wind (MW) which is southerly along the western boundary.

OSD
11, 753–788, 2014

2.2 The mathematical model

The reduced-gravity shallow water equations are used in a rectangular basin on the equatorial β-plane:

$$\partial_t u + u\partial_x u + v\partial_y u - fv + g'\partial_x \eta = \nu\nabla^2 u + \frac{C_1\tau_x}{\rho(H+\eta)}, \quad (1)$$

$$\partial_t v + u\partial_x v + v\partial_y v + fu + g'\partial_y \eta = \nu\nabla^2 v + \frac{C_2\tau_y}{\rho(H+\eta)}, \quad (2)$$

$$\partial_t \eta + \partial_x[(H+\eta)u] + \partial_y[(H+\eta)v] = 0; \quad (3)$$

here u and v represent the zonal and meridional velocities, respectively. The system is subject to a zonal and meridional wind-stress forcing τ_x, τ_y and no-slip boundary conditions. A Laplacian lateral diffusion with a viscosity ν is used. It is necessary to insure the no-slip boundary condition and its role is also to prevent the accumulation of energy/enstrophy at the smallest scales that are resolved numerically. Please see Frisch et al. (2008), for a detailed discussion of this bottleneck phenomena.

The associated equation for vorticity is:

$$\partial_t \xi + u\partial_x \xi + v\partial_y \xi + \beta v + (\xi + f)(\partial_x u + \partial_y v) - \nu\nabla^2 \xi = F, \quad (4)$$

or in conservative form:

$$\partial_t \xi + \partial_x[u(\xi + f)] + \partial_y[v(\xi + f)] - \nu\nabla^2 \xi = F, \quad (5)$$

where F is the curl of the forcing.

OSD
11, 753–788, 2014

2.3 The winds-tress forcing

The wind-stress implemented in Eqs. (1) and (2) is discriminated into a trade wind forcing $(C_1, C_2) = (4, 0)$ and a monsoon wind forcing $(C_1, C_2) = (0, 3.5)$ where we choose:

$$\tau_x = 0.1 \frac{\mathrm{N}}{\mathrm{m}^2} \left[1 - \exp\left(\frac{x}{L_x}\right)\right] \left[\exp\left(-4\left(\frac{y}{L_y}\right)^2\right)\right] \left[1 - \exp\left(\frac{-t}{t_c}\right)\right], \quad (6)$$

$$\tau_y = 0.1 \frac{\mathrm{N}}{\mathrm{m}^2} \left[\exp\left(-4\left(\frac{x}{L_x}\right)^2 - 0.2\right)\right] \left[1 - \exp\left(\frac{-t}{t_c}\right)\right]. \quad (7)$$

The values of the parameters are chosen, so that the transport in the boundary currents are similar at $y = +1500$ km for the TW and the MW forcing, for a viscosity $\nu = 1000\,\mathrm{m}^2\,\mathrm{s}^{-1}$. The spin-up time for the wind forcing is $t_c = 180$ days.

2.4 The numerical implementation

The numerical method used to solve the Eqs. (1)–(3) is a centered, second-order finite difference scheme in space and a second order Runge–Kutta scheme is used for time stepping. A fine numerical resolution of square geometry ($\Delta x = \Delta y = 2.5$ km) is employed throughout the entire domain. This uncommon choice, of not using grid refinement at the boundary, is justified by the results presented in Sect. 4, where it is clearly seen that for high Reynolds number flow, parts of the viscous sub-layer are torn of the wall and transported away from it by the surrounding turbulent flow. This leads to small scale structures also far from the boundary. Such kind of process can only be represented when there is fine resolution in both horizontal directions throughout the extended boundary layer (to be defined in Sect. 4.4). Please note that the resolution is well below the Munk scale $\delta_M = (\nu/\beta)^{1/3}$, which is around 18 km in the lowest viscosity experiment. We favor fine-resolution rather than high-order schemes. The time-step is 90 s, which is almost ten times shorter than the CFL time-step imposed by the speed

OSD
11, 753–788, 2014

of the gravity waves. In the nonlinear boundary layer the high vorticity in the boundary layer is intermittently torn of the boundary. This process is the equivalent of bursts in 3-D boundary layers (see e.g. Robinson, 1991). It is this violent process and its nonlinear evolution that asks for a short time-step.

3 Experiments

For both types of wind forcing (TW and MW) experiments for different values of the viscosity were performed. Experiments are referred to by the forcing followed by the viscosity value: MW1000 is an experiment with MW forcing and a viscosity $\nu = 1000\,\mathrm{m^2\,s^{-1}}$. The highest viscosity experiments with $\nu = 1000\,\mathrm{m^2\,s^{-1}}$ converged towards a stationary dynamics, the corresponding Reynolds number based on the maximal average meridional velocity in the boundary current and the Munk-layer thickness at $y = +1500\,\mathrm{km}$ is $Re = v_0\delta_M/\nu = 31$ and 42 for TW1000 and MW1000, respectively. The numerical resolution and scheme allowed to perform calculations with viscosities down to $\nu = 125\,\mathrm{m^2\,s^{-1}}$ for the TW forcing. For the MW forcing the lowest viscosity was $\nu = 300\,\mathrm{m^2\,s^{-1}}$. The reason for the more stable TW experiments lies in the existence of inertial effects that play a stabilizing role, as discussed in Sect. 4.4.

In the high viscosity experiments the boundary layer dynamics converges towards a stationary state in about 3000 days of the dynamics. Lower viscosity experiments converge to a statistically stationary state. To increase the significance of the statistics, experiments were performed for 5000 days of the dynamics and averages were calculated over the last 2000 days.

OSD
11, 753–788, 2014

4 Results

4.1 Large-scale circulation

For both types of wind forcing TW and MW strong western boundary currents with a recirculation in the rest of the domain were observed, as can be seen in Fig. 1. With the TW forcing the boundary current is poleward in both hemispheres. The southward boundary current is less strong due to the domain extending only 1000 km to the south but 3000 km to the north. The MW forcing led to a single gyre extending over the entire domain with the western boundary current crossing the equator in the northward direction. Another important difference between the circulation resulting from MW and TW forcing, is that for the former the boundary current is in the northern direction and the zonal velocity vanishes almost completely except near the southern and northern boundaries of the domain. While in the latter the zonal velocity is westward at low latitudes up to about $y = +1300$ km and eastward above (see Fig. 2). We will see in the sequel that these relatively small zonal velocities have an important impact on the stability and nature of the boundary current system. For the largest viscosity values, the dynamics converge towards a stationary flow for both types of wind forcing. In experiments with lower viscosities, time dependence arises in the form of coherent anticyclones moving northward along the western boundary. For the lowest viscosity experiments the dynamics are fully turbulent, with chaotic motion over a range of spacial scales (see Sect. 4.4). The time averaged large-scale circulation of the low viscosity experiments is qualitatively similar to the stationary flow at high viscosity.

4.2 Laminar boundary layers

For the high values of the viscosity the stationary solutions of the boundary layer are, to leading order, given by a balance of the meridional transport of planetary vorticity (4th term in Eq. 4) and the viscous dissipation (last term on the l.h.s. of Eq. 4). This dynamic is described by the Munk-layer theory (Munk, 1950; Pedlosky, 1990) and the

OSD
11, 753–788, 2014

solutions are:

$$v_M(x) = v_M^0 \exp\left(-\frac{x}{2\delta_M}\right) \sin\left(\frac{\sqrt{3}}{2}\frac{x}{\delta_M}\right) \quad (8)$$

where $\delta_M = (\nu/\beta)^{1/3}$ is the characteristic boundary layer thickness of the Munk-layer and v_M^0 is a velocity scale. There is a fair agreement between Munk-layer theory and our numerical results for the MW and the TW forcing at higher latitude, where inertial effects vanish, as can be seen in Fig. 2. Munk-layer theory is base on quasi-geostrophy and neglects variations in the layer thickness, which are important in our reduced-gravity model (see Sect. 4.6) at low latitude. The vortex stretching is given by the fifth term in Eq. (4). We found the vortex stretching to be important very close to the boundary but decreases rapidly before the meridional velocity reaches its maximum (not shown), but does not lead to substantial deviations from the Munk-layer and inertial-layer solutions as can be verified in Fig. 2. This is in agreement with the results of Edwards and Pedlosky (1998a). At low latitudes in the TW circulation there is a significant westward velocity. This alters completely the boundary layer structure as the vorticity balance in the outer part of the boundary layer is now between the meridional transport of planetary vorticity (4th term in Eq. 4) and the westward transport of relative vorticity (second term in Eq. 4), leading to an inertial boundary layer (Charney, 1955, see also Pedlosky, 1990 and Vallis, 2006). The outer part of the boundary layer is now much better fitted (see Fig. 2) by the inertial boundary layer solution:

$$v_I(x) = v_I^0 \exp\left(-\frac{x}{\delta_I}\right), \quad (9)$$

where $\delta_I = \sqrt{-u_I(y)/\beta}$ is the characteristic boundary layer thickness of the inertial layer and v_I^0 is a velocity scale. At the boundary the inertial solution is modified by viscous dissipation, which is necessary to satisfy the no-slip boundary condition. Such viscous dissipation is also necessary for the basin wide vorticity balance as discussed in

OSD
11, 753–788, 2014

Sect. 4.6. Note, that the inertial scale δ_I, also called the Charney scale, is a result of the large-scale dynamics due to the wind forcing. It depends only weakly on the viscosity. Whereas, the Munk-layer scale δ_M depends only on external parameters, it can be calculated independently of the circulation. When $\delta_I > \delta_M$ inertial effects govern the outer part of the boundary layer, prevent it from becoming thinner and stabilize it (see also Ierly and Young, 1991). This explains the increased stability of the equatorward part of the boundary layer in the TW circulation. Please note, that an eastward velocity has no such stabilizing effect. Indeed in the TW experiment there is a eastward average velocity in the northern part of the domain, the Charney scale becomes complex valued and a tendency to spatial and temporal oscillations are observed (see Sect. 4.6).

4.3 Coherent structures

4.3.1 Anticyclones

The most conspicuous coherent structures are the anticyclonic eddies along the western boundary. In the MW experiments they start to appear at viscosity values of $\nu = 1000\,\mathrm{m^2\,s^{-1}}$ during the spin-up as poleward travelling waves in the boundary layer. They travel northward along the boundary at a speed of $V_{\mathrm{eddy}} \approx 2.3 \times 10^{-1}\,\mathrm{m\,s^{-1}}$. This speed is faster than the fastest Rossby wave meaning that they do not radiate Rossby waves (Ierly and Young, 1991). Their size increases with a decreasing viscosity. At viscosities of $\nu \approx 500\,\mathrm{m^2\,s^{-1}}$, they are coherent regular vortices. Their diameter is then around the equatorial Rossby radius of deformation $L_\beta = \sqrt{\sqrt{g'H}/\beta} = 350\,\mathrm{km}$, a size that compares well to the size of the eddies in the Somali current (Schott and McCreary, 2001; Wirth et al., 2001) and to the eddies of the North Brazil current (Richardson and Schmitz, 1993). When inspecting the potential vorticity (PV) they appear as negative PV anomalies that move poleward with an average speed of $V_{\mathrm{eddy}} \approx 1 \times 10^{-1}\,\mathrm{m\,s^{-1}}$, while the fluid velocity in their interior reaches a speed of $v_{\mathrm{eddy}} = 2\,\mathrm{m\,s^{-1}}$. This demonstrates, that the eddies are advected water masses and not wave-like phenomena. A closer

OSD
11, 753–788, 2014

inspection of the velocity field shows that they are eddies in almost perfect solid-body rotation and not vortex rings (not shown), with an almost motionless core (eye). One has to mention that in the literature eddy or ring are often used interchangeably to denote the same object. With decreasing viscosity their shape and poleward displacement exhibit a random-like behavior (Wirth et al., 2001) as can be verified analyzing Hovmöller diagrams (not shown) indicating a chaotic dynamics. For the lower viscosity values the eddy dynamics becomes more chaotic, some of the eddies migrate into the interior of the basin, merge with other eddies or are disintegrated by them in a 2-D turbulent eddy dynamics. At the lowest viscosity value of $\nu = 300\,\mathrm{m^2\,s^{-1}}$, the average northward displacement velocity is around $V_{\mathrm{eddy}} \approx 6\times10^{-2}\mathrm{m\,s^{-1}}$, while the fluid velocity in their interior reaches speed of $v_{\mathrm{eddy}} = 2\,\mathrm{m\,s^{-1}}$.

With the TW forcing the boundary layer is stabilized by the inertial effect as discussed in Sect. 4.2 above. There are no eddies south of $y = +1000$ km, the latitudes at which the time averaged zonal velocity is negative. At higher latitudes and for a viscosity of $\nu = 1000\,\mathrm{m^2\,s^{-1}}$ a single eddy is created that migrates northward to the northwest corner of the domain, where it stabilizes. A chaotic eddy dynamics appears for the viscosities of $\nu = 500\,\mathrm{m^2\,s^{-1}}$ and below at latitudes higher than $y = +1000$ km. The eddies have an average tendency to migrate eastward and the fluid velocities reach locally up to $v_{\mathrm{eddy}} = 2.4\,\mathrm{m\,s^{-1}}$.

4.3.2 Bursts

For the lowest values of the viscosity, intermittent detachments of the viscous sub-layer just northward of the eddy center are observed at the boundary (see Fig. 3). The viscous sub-layer is the thin layer of a few tenths of kilometers thickness, for the lower viscosity values, at the boundary where the vorticity has large positive values. It is discussed in detail in Sect. 4.6 of this section. The detachments are the most violent phenomena in the simulations with the strongest velocity and vorticity gradients. When the sheet of positive vorticity along the western boundary in the Munk-layer breaks due

OSD
11, 753–788, 2014



to the action of an anticyclone, the southward part detaches, is torn of the boundary by the anticyclone and accelerates away from the boundary (see Fig. 3). North of the detachment the vorticity anomaly and the meridional velocity are negative. These events are the analog to bursts or ejections in the classical boundary layer (Robinson, 1991) and are thus given the same name here. They are strong spatially localized and temporally intermittent ejections of fluid and vorticity away from the wall, initiated by the large anticyclonic eddies. The separation of the boundary layer plays a key role in boundary layer dynamic since Prandtl (1904), see also Schlichting and Gertsen (2000).

The ejection of the boundary layer and its offshore transport, asks for fine resolution in both horizontal directions not only in the vicinity of the boundary layer but also in areas to which the boundary layer fragment is transported.

In our analysis we identify bursts as events when the meridional velocity in the viscous sub-layer is negative. Please note that the dynamics in the viscous sub-layer is not laminar, a feature that is also found in turbulent wall bounded flows in engineering applications (Robinson, 1991). To quantify the occurrence of burst, the percentage in time of the meridional velocity inversion at $y = +1000$ km is given by the T1 and the average over time and the interval $y \in [+125, +2250\,\text{km}]$ by T2 in Table 1. In the MW experiments the percentage of the meridional velocity inversion is similar at $y = +1000$ km than those of the range of latitude between $y \in [+125, +2250\,\text{km}]$ meaning that there is only a feeble dependence on latitude. In the TW experiments almost no bursts occur south of $y = +1000$ km in accord with the fact that there are no eddies south of $y = +1000$ km in the TW experiments as mentioned above (Sect. 4.3.1). For viscosities $\nu = 1000\,\text{m}^2\,\text{s}^{-1}$ or larger there are no bursts in both type of wind forcing. Bursts are observed for $\nu = 500\,\text{m}^2\,\text{s}^{-1}$ and lower in the MW experiments and for $\nu = 400\,\text{m}^2\,\text{s}^{-1}$ and lower in the TW experiments. The percentage of bursts strictly increases with decreasing viscosity in all the experiments performed and reaches values of around 20 % for the lowest values of the viscosity, showing that they are a recurrent dominant feature of low viscosity boundary currents when inertial effects are absent.

OSD
11, 753–788, 2014

4.3.3 Dipoles

In many instances the positive vorticity anomalies, ejected from the boundary during bursts, pair with negative vorticity anomalies from within the anticyclones and form dipoles (see Fig. 3) which then travel ballisticaly (at almost constant velocity) over distances of several eddy diameters. The size of the dipoles measured by the distance of the vorticity minima and maxima spans between the thickness of the viscous boundary layer δ_v (see below) and the size of the coherent anticyclones.

4.4 Scales of motion

For an understanding of the dynamics it is essential to determine the spatial scales of the turbulent motion. We consider two key quantities. The first is twice the time averaged kinetic energy (per unit mass) divided by the time averaged enstrophy (square of vorticity):

$$\lambda_1 = \sqrt{\frac{\langle u^2 + v^2 \rangle}{\langle \zeta^2 \rangle}}. \tag{10}$$

These quantity is shown in Figs. 4 and 5. In 3-D turbulence it is the Taylor-scale divided by $\sqrt{5}$ (see Frisch, 1995). This length scale characterizes the size of the velocity gradients. The second length scale is the time averaged enstrophy divided by the time averaged palinstrophy (square of the vorticity gradient):

$$\lambda_2 = \sqrt{\frac{\langle \zeta^2 \rangle}{\langle (\nabla \zeta)^2 \rangle}}. \tag{11}$$

These quantity is shown in Fig. 5. It is characteristic of the viscous dissipation lengthscale in the enstrophy cascade (Bofetta and Ecke, 2012), the smallest scales in the vortical dynamics. The separation between the two scales gives an idea of the scale

OSD
11, 753–788, 2014

range over which turbulence is active. These scales are instructive in a turbulent environment but in the boundary layer dominated by viscosity their significance is limited. At the boundary $\lambda_1 = 0$ as energy vanishes, which does not mean that we have infinitely small scales there. At high viscosity the smallest scale is given by the Munk scale δ_M even when the analytic solutions for the laminar Munk-layer are (with $x' = \sqrt{3}x/(2\delta_M)$):

$$\lambda_1 = \delta_M \sqrt{\left(\frac{2\sin(x')}{\sin(x') - \sqrt{3}\cos(x')}\right)^2} \quad \text{and} \quad \lambda_2 = \delta_M \sqrt{\left(\frac{\sin(x') - \sqrt{3}\cos(x')}{\sin(x') + \sqrt{3}\cos(x')}\right)^2}, \qquad (12)$$

which oscillate between zero and infinity. This shows that the above scales are not useful for analyzing time-independent flow. Note, that traces of these oscillations remain in the low viscosity experiments, as can be seen in Figs. 4 and 5.

Figure 4 shows the spatial distribution of the Taylor scale in the highest Reynolds number experiments for the MW and TW forcing, respectively. A striking feature is the wide extension of the low-size values into the interior of the domain in both cases, the feeble variation within this domain and the sudden jump to high values at its clearly defined boundary as seen in Figs. 4 and 5. A clear plateau at around a scale of 60 km is observed which extends of up to 2000 km into the interior of the domain. We call the area of the plateau, the extended boundary layer (EBL). The scale of 60 km is easily explained by the eddy size of 400 km $\approx 2\pi 60$ km. Figure 5 shows that the width of the extended boundary layer is increasing with decreasing viscosity. The dissipation length scale λ_2 is smallest near the boundary and increases slowly there after, approaching the Taylor scale. When λ_2 reaches the eddy scale λ_1, the velocity gradients are dissipated and turbulence disappears. The behavior of both scales, λ_1 being constant and λ_2 increasing by barely a factor of two through the extended boundary layer, shows that grid refinement near the boundary might be useful in laminar, low Reynolds number simulations, but is not adapted for the fully turbulent case where small scale structures dominate throughout the extended boundary layer. The zonal extension of the extended boundary layer increases with a decreasing viscosity as shown in Fig. 8 and quantified

OSD
11, 753–788, 2014

in Sect. 4.6. Supposing a scaling behavior for the extension of the extended boundary layer with viscosity in the MW forcing experiments suggests an exponent close to $-2/3$ as shown in Table 2. An exponent that we can not explain. A striking feature is that, although the extension of the extended boundary layer depends on viscosity, the scales within it appear almost independent of it, once the viscosity is low enough to allow for turbulent motion. Turbulent motion in the extended boundary layer is likely to include the range of scales from λ_1 down to λ_2.

It is important to notice that in our calculations λ_2 is always more than 5 times the grid size showing that the dynamics is numerically well resolved in our calculations.

4.5 Moments of the velocity field

After having discussed the time averages of the velocity components, we will now focus on higher order moments of the fluctuations of these components. We suppose that the dynamics is in a statistically stationary state and we separate the variables into a time average and a perturbation that is: $a = \langle a \rangle + a'$. The higher order moments of the velocity components are given in Fig. 6, where they are also compared to the moments of a disc of radius R in anticylonic solid-body rotation. Taking the averages of moments of the velocity fluctuations in the y-direction over the disc, is equivalent to taking time averages at one y-location of a disc (or a succession of disks) transported by a mean flow in the y-direction at constant velocity. The comparison, presented in Fig. 6, shows that major aspects of the turbulent fluxes can be, to a good accuracy, explained by the anticyclonic discs in solid-body rotation. This confirms, that the anticyclones are the dominant coherent structures.

The positive value of $\langle u'^3 \rangle$, however, can not be explained by the disc model, which leads to a vanishing third order moment. It is a signature of the bursts and dipoles, with more intense and localized transport away from the boundary than the recirculation towards the boundary. This agrees with the findings of anisotropic burst and dipole dynamics in Sect. 4.3.

OSD
11, 753–788, 2014

4.6 Vorticity fluxes

The vorticity balance in the laminar, time independent, boundary layer is described in Sect. 4.2. In the unstable boundary layer the vorticity balance changes. When time averaging is applied to Eq. (5) it transforms to:

$$\partial_x \left[\langle u\rangle\langle\xi\rangle\right] + \partial_y \left[\langle v\rangle\langle\xi\rangle\right] + \partial_x\langle u'\xi'\rangle + \partial_y\langle v'\xi'\rangle + \beta\langle v\rangle + f(\partial_x\langle u\rangle + \partial_y\langle v\rangle) - \nu\nabla^2\langle\xi\rangle = \langle F\rangle. \quad (13)$$

In a statistically stationary state a time average of an integration of the advection of vorticity over a closed basin vanishes and the integral balance is between the forcing (r.h.s of Eq. 13) and the viscous vorticity flux through the boundary (last term on the l.h.s. of Eq. 13). Within the basin the advection of vorticity can connect the (basin-wide) source to the sink. The different terms in the l.h.s of Eq. (13) correspond to the relative vorticity advection (RVA, terms 1 and 2), turbulent relative vorticity advection (TRVA, terms 3 and 4), planetary vorticity advection (PVA, term 5), stretching (STR, term 6) and vorticity dissipation (FRIC, term 7). The stretching term is negligible and does not contribute significantly to the vorticity the balance (see Fig. 7). For high viscosities the local vorticity balance in the boundary layer is, to leading order, between the planetary vorticity advection (term 5) and the vorticity dissipation (term 7), leading to a Munk-layer as discussed in Sect. 4.2 of this section. When the viscosity is reduced the RVA and TRVA play an increasing role in the vorticity balance. The advection of relative vorticity spatially connects the transport of planetary vorticity and the viscous dissipation and both can exhibit a different zonal length scale. This is clearly visible in Fig. 7: the FRIC dominates in a narrow region near the boundary, whereas the PVA extends further from the boundary. We call the area of the viscous dissipation the viscous sub-layer (VSL) while we choose the expression "advective boundary layer" (ABL) for the wider area of large average meridional velocity. The thickness of the former is denoted by δ_ν while the thickness of the latter is given by the symbol δ_V. In the Munk-layer theory they both coincide $\delta_\nu = \delta_V = \delta_M$. We estimate the thickness of the viscous sub-layer

OSD
11, 753–788, 2014

by the distance from the boundary at which the absolute value of the Laplacian of the average vorticity has reduced to a third of its maximal value. The same criterion was applied to the average meridional velocity to obtain δ_V. Results for the corresponding boundary layer scales for the MW and TW cases and at different latitudes as a function of viscosity are assembled in Fig. 8. For the viscous sub-layer results show that its thickness drops well below the Munk-scale for the lower viscosities, while the thickness of the advective boundary layer is always above. The advection of relative vorticity can be decomposed into the advection of the average vorticity by the average velocity field (RVA), which we call inertial contribution, and the turbulent transport of vorticity (TRVA). The difference between the TW and the MW circulation at low latitude is that, for the former the inertial terms are important while for the later the turbulent terms transport the vorticity. This explains the laminar boundary layer of the TW circulation at low latitude and the turbulence of the MW boundary layer. Please note that the inertial boundary layer in the TW circulation stays laminar even for the smallest viscosity used, if it becomes turbulent at even lower viscosities, is an open question. This behavior is clearly depicted in Fig. 7, where at low latitudes of the TW circulation the inertial part connects the planetary vorticity advection to the viscous dissipation, whereas at higher latitudes and for the MW circulation it is the turbulent advection. Please note that Ierly and Young (1991) propose a scaling of $\delta_\nu \sim \nu^{1/6}$ for the boundary layer with an inertial component based on laminar boundary layer theory and an ansatz for the shape of the boundary layer. We analyzed the scalings of the turbulent boundary layer thickness by considering values obtained from turbulent boundary layers. Our results for the inertial boundary layer, see Table 2, show a much steeper scaling of $1/2$ at low latitudes. This exponent suggests that the dominant vorticity advection near the boundary does not depend on the viscosity and has to be balanced at the boundary by viscous dissipation. At higher latitudes the scaling is higher for the TW forcing, showing that the boundary layer thickness decreases even faster with decreasing viscosity, when "inverse inertial" effects are present. In Fig. 7 the inertial part shows an oscillatory behavior at high

OSD
11, 753–788, 2014

latitudes for the TW forcing, where the zonal velocity is positive, which leads to an inertial boundary layer scale that is complex valued, which explains the oscillations.

The scaling of the advective boundary layer thickness δ_V for the MW forcing shows a slight increase with decreasing viscosity (see Table 2) and a possible saturation around 200 km. For the TW forcing δ_V shows a slight decrease with decreasing viscosity at low latitude and a saturation at the value corresponding to the inertial boundary layer. At higher latitude, where an inverse inertial boundary layer is present, the thickness of the advective boundary layer still increases with decreasing viscosity.

4.7 Estimation of the eddy viscosity via the Munk formula

We have shown in Sect. 4.2 and Fig. 2 that the profile of the meridional velocity in the stationary boundary layer is close to the shape of the Munk-layer, when inertial effects are absent. When turbulence is present the shape of the time averaged meridional velocity still somehow resembles the Munk-layer solution with the meridional velocity vanishing at a distance x_0 from the boundary. For the Munk layer we have $x_0 = (2\pi/\sqrt{3})\delta_M$. The meridional gradient in layer thickness (s) imposed by the large-scale circulation adds a topographic $\beta_{topo} = -fs/H$ to the planetary value. Its value depends only weakly on the viscosity. When the effective β-term, composed of the planetary and topographic part, is constant, the Munk-layer scale is proportional to the cubic-root of the (eddy) viscosity and so is x_0. The idea is now to calculate an eddy viscosity ν_{eddy} based on x_0. To this end we measure the value x_0 in an experiment with high viscosity $\nu_{stat} = 1000\,m^2\,s^{-1}$ that has a time-independent dynamics and compare it to the value obtained from the average of a turbulent experiment at the same latitude. The eddy viscosity can then be obtained by using the proportionality:

$$\nu_{eddy} = \left(\frac{x_0}{x_0(\nu_{stat})}\right)^3 \nu_{stat}. \quad (14)$$

Such method can not be applied to the inertial boundary layer as, in this case the average meridional velocity decays exponentially away from the boundary and does not

OSD
11, 753–788, 2014

vanish. The following analysis was not applied to the inertial boundary layer. A clear scaling for $v'_{\text{eddy}} = \nu_{\text{eddy}} - \nu$ as a function of the zonal maximum of the r.m.s. velocity fluctuations $u'_{\text{r.m.s.}}$ is observed in Fig. 9, for data from the MW and TW forcing at higher latitudes. The scatter plot is well fitted by an affine regression line of equation

$$v'_{\text{eddy}} = \nu_{\text{eddy}} - \nu = u'_{\text{r.m.s.}} \cdot 6283.3\,\text{m} - 639.3\frac{\text{m}^2}{\text{s}}, \tag{15}$$

which means that whatever the forcing and the viscosity, there is a correlation between the eddy viscosity and the fluctuating velocity. The correlation of the best fit linear regression is $R = 0.97$. The finding that for small values of $u'_{\text{r.m.s.}}$ there is no turbulent contribution to the eddy viscosity is explained by the fact, that the small perturbations have a wave-like structure which do not lead to turbulent fluxes.

The simplest way to estimate a eddy viscosity proposed by Prandtl (1925) Mischungsweg (mixing length) λ and the fluctuating velocity $u'_{\text{r.m.s.}}$ is:

$$v'_{\text{eddy}} = \nu_{\text{eddy}} - \nu = \alpha\lambda_1 u'_{\text{r.m.s.}} \tag{16}$$

The results of the nonlinear experiments confirm this proportionality. For our data and $\lambda_1 = L_{\text{eddy}}/(2\pi) = 60\,\text{km}$ calculate previously we obtain $\alpha \approx 0.1$. If we suppose, that the eddy viscosity is due to the anticyclones this value of α is within the range proposed by Smagorinsky (1993). The values of λ_1 and $u'_{\text{r.m.s.}}$ can not be obtained from external parameters but are a result from the numerical experiment. In concrete cases, they can often be obtained from observation or fine resolution numerical simulations.

Using $\alpha = 0.1$ and the typical values for the Somali current of $L_{\text{eddy}} = 400\,\text{km}$ and $u'_{\text{r.m.s.}} = 1\,\text{m}\,\text{s}^{-1}$ leads to $\nu_{\text{eddy}} \approx 6000\,\text{m}^2\,\text{s}^{-1}$ and a $\delta_{\text{Munk}} \approx 70\,\text{km}$. A consequence of this is that even a non-eddy permitting ocean model should have a grid size not exceeding 50 km to capture the boundary layer dynamics and the associated meridional heat transport at least in an average sense and no value of the eddy viscosity larger than $6000\,\text{m}^2\,\text{s}^{-1}$ should be used.

OSD
11, 753–788, 2014

This pragmatic approach leads to a viscosity and a boundary layer thickness that compares well to average values in the turbulent boundary current. This approach is of course questionable as the eddy size is larger than the mean current, that is the scale separation is smaller than unity and the eddy viscosity approach asks for large scale-separations. This problematic was already noticed by Charney (1955) who states: "In order to account for the observed width of the current, Munk was forced to postulate an eddy viscosity so large that the eddy sizes were themselves comparable to the width."

We have estimated the eddy viscosity based on the average meridional velocity and have shown, that it can be connected via Prandtl's formula to the velocity fluctuations. This is however not a parameterization as the turbulent fluxes themselves are not obtained from the large-scale dynamics.

5 Discussion and conclusions

In the MW forcing case the boundary current crosses the equator and we have not observed that the vanishing of the Coriolis parameter at the equator plays a special direct role in the dynamics of western boundary currents. In the TW forcing case the equatorial current splits up and flows poleward in both hemispheres as a western boundary current. In our calculations the importance of the equator is due to the larger latitudinal velocities (inertial effect) and the unstable wave dynamics at the equator, which increases the variability, also at the western boundary.

Without the stabilizing inertial effects, the transport of PV towards the boundary area, the western boundary layer does not exist for high Reynolds number flow. The western boundary is a turbulent region with interacting eddies, bursts and dipoles and frequent velocity inversions. Its boundary layer structure can only be recovered in an average sense. The turbulent dynamics leads to a split up of the boundary layer into three layers: a viscous sub-layer, an advective boundary layer and an extended boundary layer. The thickness of the first and the third are, respectively, decreasing and increasing when the

OSD
11, 753–788, 2014

viscosity is decreased. The second shows no or only a weak dependence on viscosity, once it drops below values that allow for turbulent motion.

We identified for the lower values of the viscosity a sequence in the evolution of the dynamics of the coherent structures: anticyclones are generated by instability, during their northward migration they intermittently detach parts of the viscous sub-layer containing strong positive vorticity, these bursts pair with negative vorticity from within the anticyclones and form dipoles which then travel ballisticaly (at almost constant velocity) over distances of several eddy diameters. In observations and a fine resolution Ocean General Circulation Models bursts are seen to lead to substantial upwelling of cold and nutrient rich water-masses from the deep. The dipole transports these water-masses offshore, leading to an increased biological production several hundreds of kilometers from the coast (Kawamiya and Oschlies, 2003; Wirth et al., 2001).

We showed that the turbulent eddy dynamics is the natural state of the high Reynolds number low latitude western boundary current. In this perspective, the question is not why eddies are present, but to the contrary, how inertial effects allow for the existence of a coherent western boundary current.

When a flat boundary is used, the thickness of the viscous sub-layer goes to zero with viscosity. A rough boundary introduces a lower bound for the thickness of the boundary.

5.1 Conclusions concerning numerical simulation of turbulent boundary layers

It is the thickness of the viscous sub-layer that imposes the spatial resolution of a numerical model. The thickness of the turbulent viscous sub-layer decreases faster with decreasing viscosity than the prominent $\frac{1}{3}$ scaling from Munk-layer theory, in all our experiments performed and at all latitudes considered. The laminar Munk-layer theory is however used to determine the (hyper) viscosity for a given spatial resolution in todays simulations of the ocean dynamics. The here presented results prove, that for the turbulent boundary layer the thus obtained resolution is far from being sufficient. The lower values for the viscous sub-layer in the MW forcing experiments as compared to the TW

OSD
11, 753–788, 2014

forcing experiments, for the same viscosity, explain also the result that experiments of the MW forcing were only possible down to $\nu = 300\,\mathrm{m^2\,s^{-1}}$ while the experiments with the TW forcing converged down to $\nu = 125\,\mathrm{m^2\,s^{-1}}$.

From Fig. 8 it is clear that the gap between the thickness of the extended boundary layer and the viscous sub-layer widens with increasing Reynolds number. The gap is a measure of the complexity of the numerical calculations as the finest scale δ_ν has to be resolved throughout δ_{ext} in both horizontal directions. This shows that grid refinement near the boundary has no place in simulations of the turbulent boundary layer as: (i) the structures are almost isotropic and (ii) the small scales extend far from the boundary. The ratio $N = (\delta_{\mathrm{ext}}/\delta_\nu)^2$ can be taken as a measure for the involved degrees of freedom in the calculations. Estimations based on our results in Table 2 clearly show a strongly increase with the Reynolds number, $N \propto Re^{2.4}$ in the low latitude MW forcing and up to $N \propto Re^{2.9}$ for the high latitude TW forcing. The scaling based on Munk-layer thickness leads to $N \propto Re^{2/3}$.

5.2 Conclusions concerning the parameterization of the turbulent boundary layers

One of the major challenges in the numerical simulation of the ocean dynamics is to parameterize the effect of the small scale dynamics not explicitly resolved on the explicitly resolved large-scale flow.

Inertial theory and the above presented results teach us that small westward velocities can stabilize the western boundary layer. Velocity components in other directions have no such effect. A parameterization of the turbulence must therefore reflect this anisotropy. The instability of the boundary layer is also strongly dependent on details of the velocity profile as noted by Ierly and Young (1991). Topographic features are also likely to play an important role in the stability and turbulent fluxes.

Our determination of the eddy viscosity in Sect. 4.7 are not a parameterization as the eddy viscosity is not obtained from large-scale properties of the flow, but from

OSD
11, 753–788, 2014

fine resolution simulations. These show that for the lowest viscosities, δ_V saturates at a value corresponding to $\nu \approx 6000\,\mathrm{m^2\,s^{-1}}$. Choosing viscosity values lower than $\nu \approx 6000\,\mathrm{m^2\,s^{-1}}$ but above the threshold for fully turbulent boundary layers $\nu \approx 300\,\mathrm{m^2\,s^{-1}}$ leads to an unreal thin average boundary layer thickness, worsening of the representation of the advective boundary layer dynamics. In numerical simulations of the boundary layer dynamics one should either simulate the turbulent dynamics or parameterize it. Our findings discussed above suggest to either use fine resolutions and viscosities below $\nu \approx 300\,\mathrm{m^2\,s^{-1}}$ and perform large-eddy simulations or larger viscosity $\nu \approx 6000\,\mathrm{m^2\,s^{-1}}$.

In our simulations we varied the eddy-viscosity parameter by roughly an order of magnitude. The corresponding necessary spatial resolutions vary from those of todays coarse resolution climate models down to those of fine resolution regional models. Even lower viscosity values lead to smaller boundary layer scales and higher velocities. At smaller scales the hydrostatic approximation, on which the shallow water equations are based is no longer valid as the dynamics becomes truly three-dimensional. Higher velocities lead to Froude numbers exceeding unity, hydraulic jumps occur and the flow becomes fully three dimensional such phenomena can not be explicitly resolved by the two-dimensional shallow water equations. In Fox-Kemper and Pedlosky (2004) and Fox-Kemper (2004) this problems are bypassed by using a constant depth model, where Froude number vanishes and by increasing the viscosity in the vicinity of the boundary. We propose here a numerical value, based on the Prandtl formula, for the eddy viscosity in the vicinity of the boundary that leads to a laminar boundary layer mimicking (on average) the dynamics of turbulent boundary layers at lower viscosity.

We did not consider the more involved behavior of hyper dissipation operators (hyper-viscosity, powers of the Laplacian), which ask for boundary conditions for derivatives of the velocity field and which lead towards thermalization at small scales of the turbulent dynamics as explained by Frisch et al. (2008).

OSD
11, 753–788, 2014

Acknowledgements. We would like to thank Bernard Barnier, Yves Morel and Guillaume Roullet for discussion. Akuetevi was funded by "Ministère de l'enseignement supérieur et de la recherche".

This work has been supported by a grant from Labex OSUG@2020 (Investissements d'avenir – ANR10 LABX56).

References

Bofetta, G. and Ecke, R.: Two-dimensional turbulence, Annu. Rev. Fluid Mech., 44, 427–451, 2012. 765

Charney, J.: The Gulf stream as an inertial boundary layer, P. Natl. Acad. Sci. USA, 41, 731–740, 1955. 761, 772

Edwards, C. A. and Pedlosky, J.: Dynamics of nonlinear cross-equatorial flow. Part 1: The tropically enhanced instability of the western boundary current, J. Phys. Oceanogr., 28, 2382–2406, 1998a. 755, 761

Edwards, C. A. and Pedlosky, J.: Dynamics of nonlinear cross-equatorial flow. Part 2: The tropically enhanced instability of the western boundary current, J. Phys. Oceanogr., 28, 2407–2417, 1998b. 755

Fox-Kemper, B.: Wind-driven barotropic gyre II: effects of eddy and low interior viscosity, J. Mar. Res., 62, 195–232, 2004. 775

Fox-Kemper, B.: Reevaluting the roles of eddies in multiple barotropic wind-driven gyres, J. Phys. Oceanogr., 35, 1263–1278, 2005. 755

Fox-Kemper, B. and Pedlosky, J.: Wind-driven barotropic gyre I: circulation control by eddy vorticity fluxes to an enhanced removal region, J. Mar. Res., 62, 169–193, 2004. 775

Frisch, U.: Turbulence: the Legacy of A. N. Kolmogorov, Cambridge University Press, 1995. 765

Frisch, U., Kurien, S., Pandit, R., Pauls, W., Ray, S., Wirth, A., and Zhu, J.-Z.: Hyperviscosity, galerkin truncation, and bottelnecks in turbulence, Phys. Rev. Lett., 101, 144501, doi:10.1103/PhysRevLett.101.144501, 2008. 757, 775

Ierly, G. R. and Young, W. R.: Viscous instabilities in the western boundary layer, J. Phys. Oceanogr., 21, 1323–1332, 1991. 755, 762, 769, 774

OSD

11, 753–788, 2014

Kawamiya, M. and Oschlies, A.: An eddy-permitting, coupled ecosystem-circulation model of the Arabian Sea: comparison with observations, J. Marine Syst., 38, 221–257, 2003. 755, 773
Munk, W. H.: On the wind-driven ocean circulation, J. Meteorol., 7, 79–93, 1950. 760
Pedlosky, J.: Geophysical Fluid Dynamics, 2nd Edn., Springer, 1990. 760, 761
Prandtl, L.: Über Flüssigkeitsbewegung bei sehr kleiner Reibung, Coll. Works, II, 575–584, 1904. 755, 764
Prandtl, L.: Bericht über Untersuchungen zur Ausgebildeten Turbulenz, Z. Angew. Math. Mech., No. 5, 136–169, 1925. 771
Richardson, P. L. and Schmitz, W. J.: Deep cross-equatorial flow in the Atlantic measured with SOFAR floats, J. Geophys. Res., 98, 8371–8387, 1993. 762
Richardson, P. L., Hufford, G. E., Limeburner, R., and Brown, W.: North Brazil current retroflection eddies, J. Geophys. Res., 99, 5081–5093, 1994. 754
Robinson, S. K.: Coherent motions in the turbulent boundary layer, Annu. Rev. Fluid Mech., 23, 601–663, doi:10.1146/annurev.fl.23.010191.003125, 1991. 759, 764
Schlichting, H. and Gertsen, K.: Boundary-Layer Theory, Springer Verlag, 2000. 764
Schott, F. and McCreary, J.: The monsoon circulation of the Indian Ocean, Prog. Oceanogr., 51, 1–123, 2001. 754, 755, 762
Smagorinsky, J.: Some historical remarks on the use of nonlinear viscosities, in: Large Eddy Simulation of Complex Engineering and Geophysical Flows, edited by: Galperin, B. and Orszag, S. A., Cambridge University Press, 3–36, 1993. 771
Vallis, G.: Atmospheric and Oceanic Fluid Dynamics, Cambridge Univ. Press., 2006. 761
Wirth, A., Willebrand, J., and Schott, F.: Variability of the Great Whirl from observations and models, Deep-Sea Res.-Pt. II, 49, 1279–1295, 2001. 754, 755, 762, 763, 773

OSD
11, 753–788, 2014

Table 1. Percentage in time of the meridional velocity inversion in the viscous sub-layer at $y = +1000$ km (T1) and for $y \in [+125, +2250$ km] (T2).

Experiments	TW125	TW150	TW250	TW300	TW400	TW500	TW1000
T1 (%)	0.93	0.8	0	0	0	0	0
T2 (%)	15.57	11.62	4.81	2.63	0.52	0	0
Experiments				MW300	MW400	MW500	MW1000
T1 (%)				21.67	17.5	13.57	0
T2 (%)				19.07	14.36	10.38	0

OSD
11, 753–788, 2014

Table 2. Scaling exponents for the zonal extension of the viscous sub-layer (VSL) thickness, the advective boundary layer (ABL) thickness and the extend boundary layer (EBL) thickness at different latitudes y for the MW forcing and the TW forcing.

y (km)	MW			TW		
	VSL	ABL	EBL	VSL	ABL	EBL
+750	0.50	−0.07	−0.68	0.50	0.13	–
+1000	0.50	−0.17	−0.63	0.50	0.08	–
+1500	0.39	−0.17	−0.71	0.89	−0.27	−0.48
+2000	0.71	−0.15	−0.62	1.20	−0.57	−0.25

OSD
11, 753–788, 2014

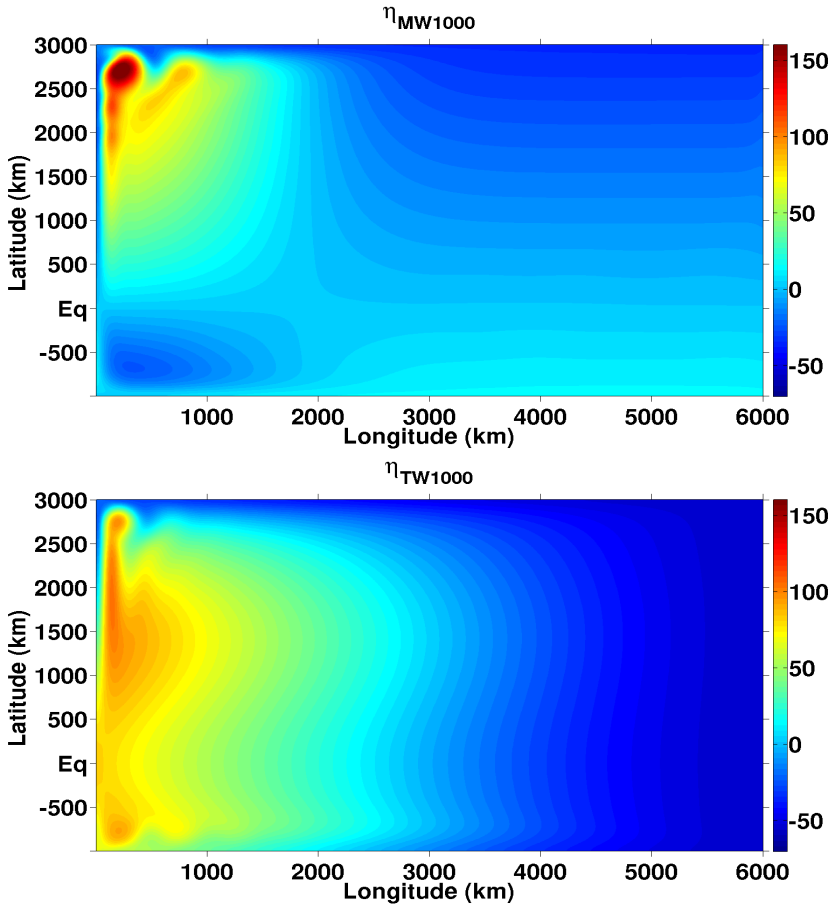

Fig. 1. Instantaneous contours of layer thickness variation at time t = 2000 days for MW1000 (above) and TW1000 (below).

OSD
11, 753–788, 2014

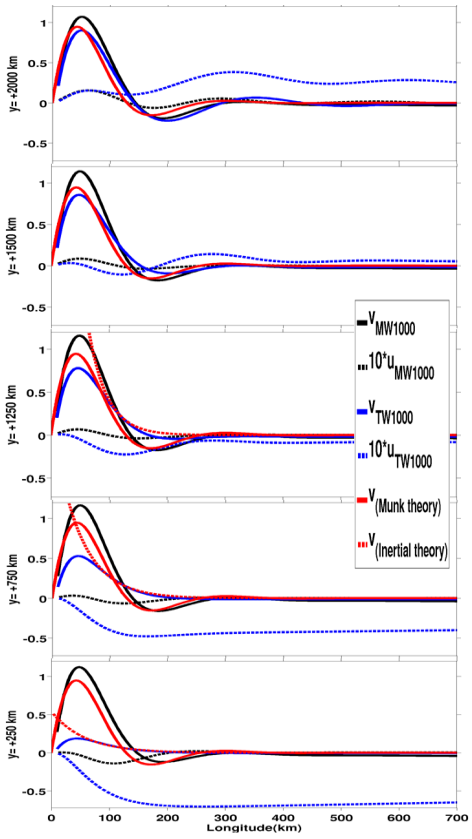

Fig. 2. Zonal profiles of the u and v components for the experiments MW1000 and TW1000 at five latitudes, $y = +2000$, $y = +1500$, $y = +1250$, $y = +750$ and $y = +250$ km from top to bottom. Superposed are the zonal profiles of the analytic solutions of Munk-layer theory (red full line) and the analytic solution of inertial-layer theory (red dashed line). The amplitudes v_M^0 in Eq. (8) and v_I^0 in Eq. (9) are chosen to best fit the data.

OSD
11, 753–788, 2014

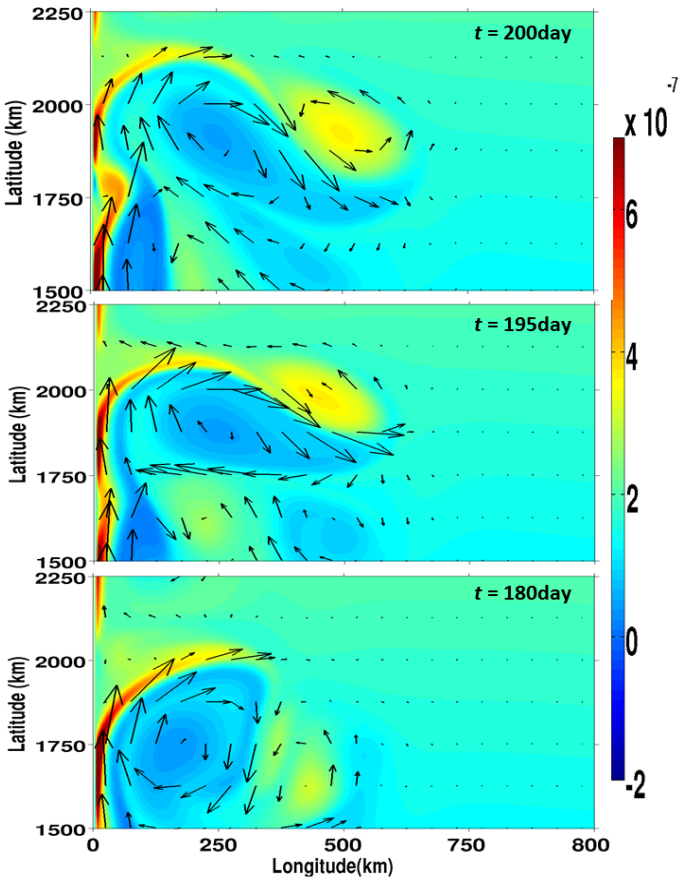

Fig. 3. Sequence of potential vorticity ($m^{-1}\,s^{-1}$) snapshots showing bursts and its subsequent development into a dipole for MW300 experiment. The snapshots were taken at t = 180, 195 and 200 days, from top to bottom.

OSD
11, 753–788, 2014

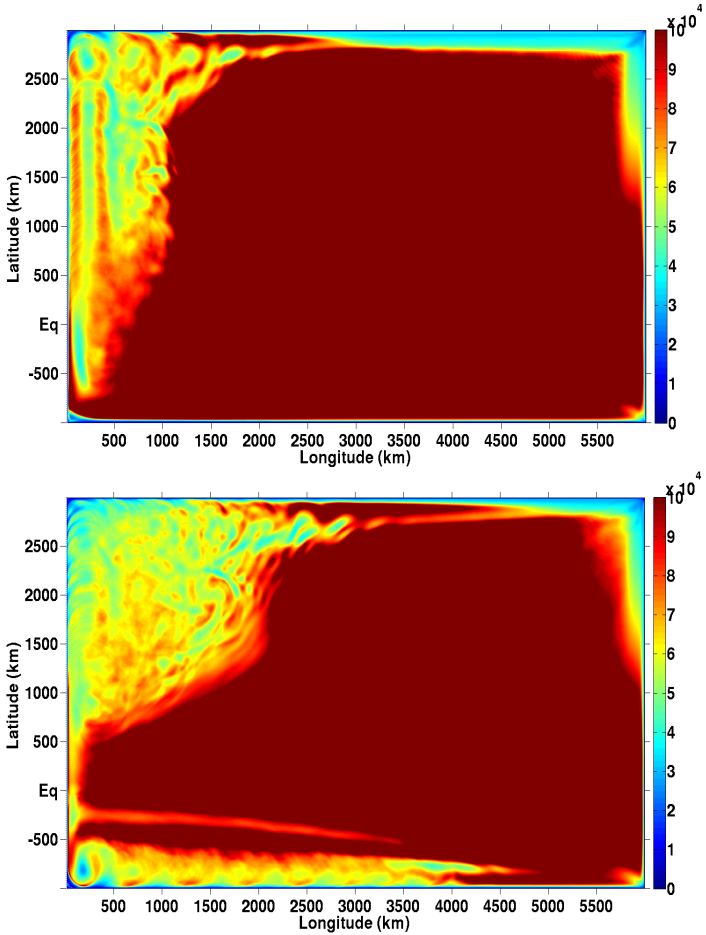

Fig. 4. Taylor scale λ_1 (m) for MW300 (above) and TW125 (below). Note that the color-bar stops at 100 km to emphasize the behavior in the extended boundary layer.

OSD
11, 753–788, 2014

Dynamics of turbulent western boundary currents

C. Q. C. Akuetevi and A. Wirth

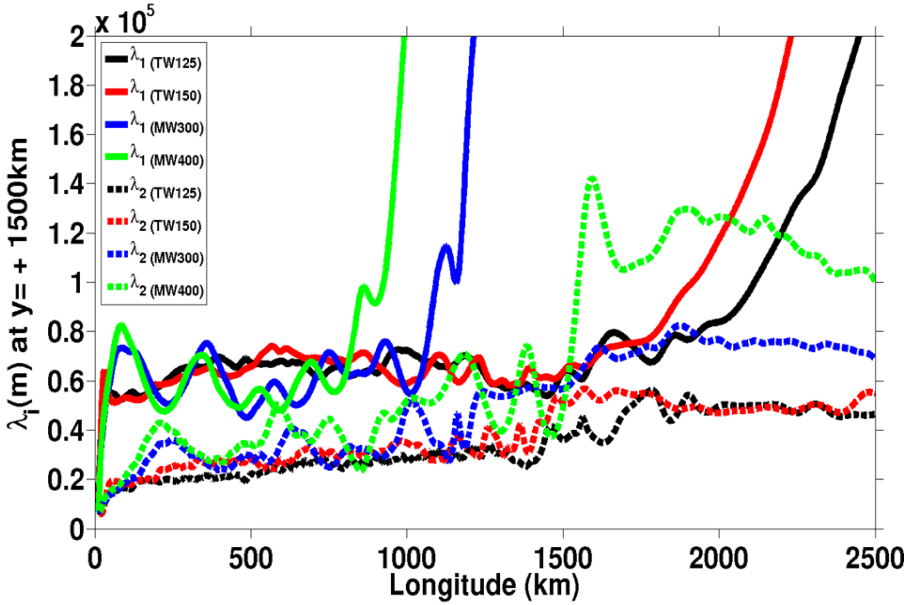

Fig. 5. Zoom of zonal profiles of Taylor scale λ_1 and small-scale λ_2 at y = +1500 km for TW125, TW250, MW300 and MW400.

OSD
11, 753–788, 2014

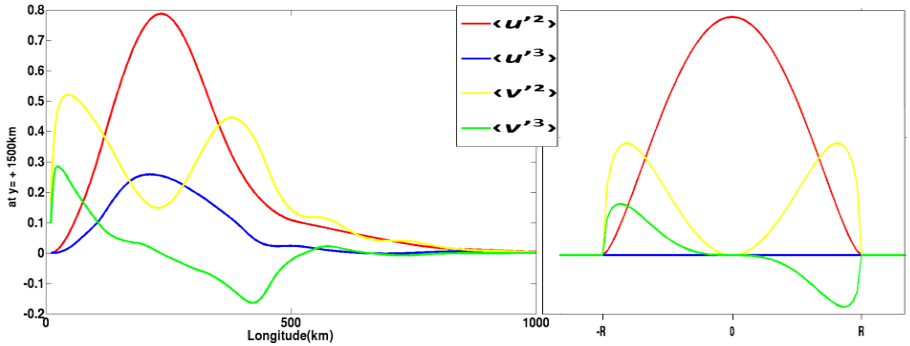

Fig. 6. Second and third order moments of the fluctuations of the velocity components from MW300 at $y = +1500$ km as a function of the distance from the boundary (left). And the analytic solutions of the same quantities for a disc in anticyclonic solid-body rotation (right).

OSD
11, 753–788, 2014

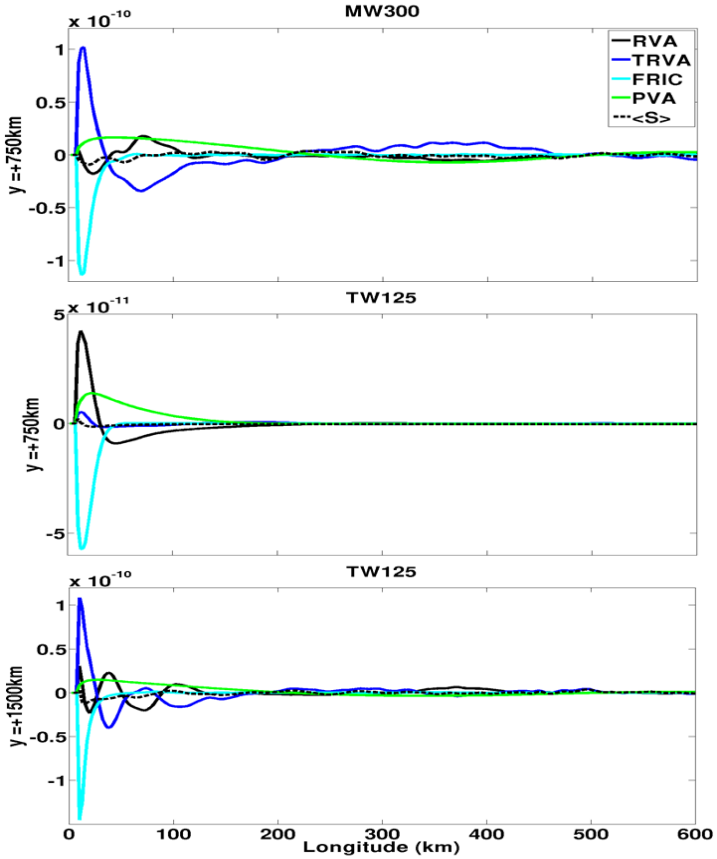

Fig. 7. Vorticity balance. Different terms of Eq. (13) are plotted for the MW300 experiment at y = +750 km (upper figure) and for the TW125 experiment at y = +750 km (middle figure) and y = +1500 km (bottom figure). $\langle S \rangle$ comprises forcing, stretching and residual time dependence.

OSD
11, 753–788, 2014

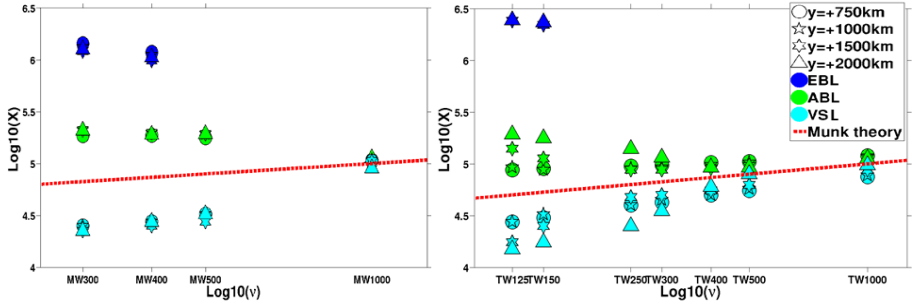

Fig. 8. Thickness of the viscous sub-layer (VSL), the advective boundary layer (ABL) and the extended boundary layer (EBL) for MW forcing (left) and TW forcing (right) experiments at different latitudes y.

OSD
11, 753–788, 2014

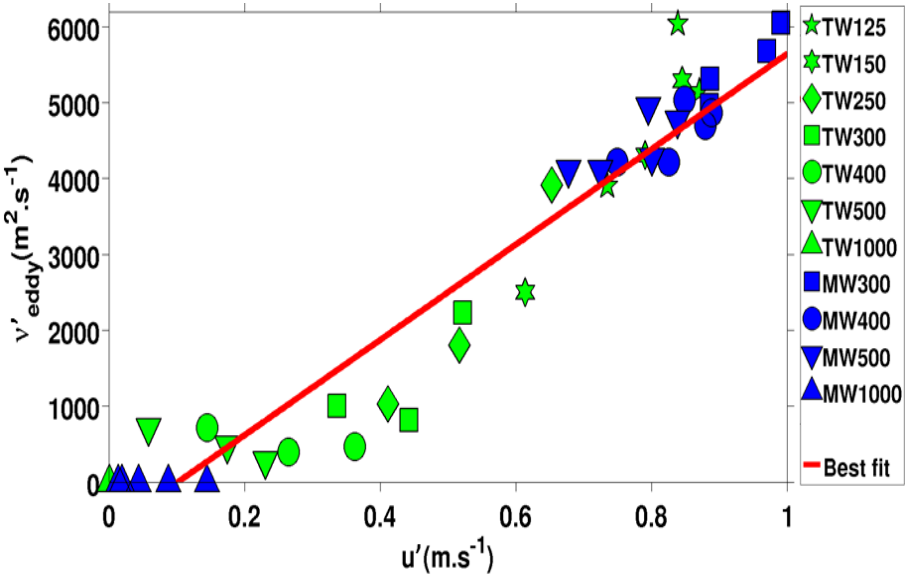

Fig. 9. Scatter plot diagram of eddy viscosity $\nu'_{\text{eddy}} = \nu_{\text{eddy}} - \nu$ computed from the data using the Munk formula approach of Eq. (14), as function of the maximum fluctuating velocity for all the nonlinear experiments at high latitudes $y = +1500$, $y = +1750$ and $y = +2000$ km. The green symbols represent the experiments with TW forcing and the blue ones those of MW forcing and the red line is the best fit affine regression line.

OSD
11, 753–788, 2014